Materials & Design 247 (2024) 113395

Contents lists available at ScienceDirect

Materials & Design

journal homepage: www.elsevier.com/locate/matdes

# 3D printed polymeric stent design: Mechanical testing and computational modeling

Francesc Canalejo-Codina [a,b,c], Mariola Cano-Morenilla [d], Jordi Martorell [b], Mercedes Balcells [b,c], Marta Pegueroles [d], Andrés A. García-Granada [a,*]

[a] Industrial Product Engineering Group (GEPI), IQS School of Engineering, Universitat Ramon Llull, Barcelona, Spain
[b] Vascular Engineering and Applied Biomedicine Group (GEVAB), IQS School of Engineering, Universitat Ramon Llull, Barcelona, Spain
[c] Institute for Medical Engineering and Science, Massachusetts Institute of Technology, Cambridge, MA, USA
[d] Biomaterials, Biomechanics and Tissue Engineering Group, Department of Materials Science and Engineering, Center for Research in Multiscale Science and Engineering (CCEM) and Research Center for Biomedical Engineering (CREB), Universitat Politècnica de Catalunya, EEBE, Barcelona, Spain

ARTICLE INFO

*Keywords:*
Additive manufacturing
Bioresorbable stent
Poly(L-lactide-co-ε-caprolactone)
Mechanical performance
Crush resistance
Finite element analysis

ABSTRACT

Polymer-based bioresorbable scaffolds (BRS) aim to reduce the long-term issues associated with metal stents. Yet, first-generation BRS designs experienced a significantly higher rate of clinical failures compared to permanent implants. This prompted the development of alternative scaffolds, such as the poly(L-lactide-co-ε-caprolactone) (PLCL) solvent-casted stent, whose mechanical performance has yet to be addressed. This study examines the mechanical behavior of this novel scaffold across a wide range of parallel and radial compression diameters. The analysis highlights the scaffold's varying responses under different loading conditions and provides insights into interpreting simulation model parameters to accurately reflect experimental results.

Stents demonstrated a parallel crush resistance of 0.11 N/mm at maximum compression, whereas the radial forces were significantly higher, reaching up to 1.80 N/mm. Additionally, the parallel test keeps the stent in the elastic regime, with almost no regions exceeding 50 MPa of stress, while the radial test causes significant structural deformation, with localized plastic strain reaching up to 30 %. Results showed that underestimating yield strain in computational models leads to discrepancies with experimental results, being 5 % the most accurate value for matching computational and experimental results for PLCL solvent-casted stents.

This comprehensive approach is vital for optimizing BRS design and predicting clinical performance.

## 1. Introduction

A vascular stent is an expandable mesh-like tube that serves as a scaffold [1], maintaining the luminal patency of a constricted artery[2] so that blood can flow smoothly without any obstruction [2,3]. These structures fall into two main categories [4]: I) permanent bare metal stents (BMS) or drug-eluting stents (DES); and II) bioresorbable stents (BRS).

Original BMS were challenged by tissue hyperplasia, which led to restenosis as the lumen often became reobstructed [5,6,7]. This challenge was partially alleviated by DES, which elute antiproliferative agents from polymer-coated metallic struts, effectively inhibiting excessive tissue proliferation and enhancing the effectiveness in reestablishing vascular patency [8,9]. However, there is a persistent concern surrounding the permanent presence of metal-based stents within the artery, which may hinder complete vascular healing. The inherent constraints linked with BMS and DES prompted the medical community to turn their attention to BRS for a solution [10,11].

BRS are bioresorbable polymeric or metallic stents, engineered to offer temporary radial support within the constricted vessels, gradually dissolving over time, thereby mitigating long-term complications associated with permanent implants [12]. Unfortunately, studies show that arteries with BRS clot two to three times more often than those with permanent stents, increasing the risk of thrombosis and myocardial infarction [13]. Consequently, researchers have explored alternative materials, geometries and fabrication techniques to address these

* Corresponding author at: Industrial Product Engineering Group (GEPI), IQS School of Engineering, Universitat Ramon Llull, Via Augusta 390, 08017 Barcelona, Spain.
*E-mail addresses:* francesccanalejoc@iqs.url.edu (F. Canalejo-Codina), mariola.cano@upc.edu (M. Cano-Morenilla), jordi.martorell@iqs.url.edu (J. Martorell), merche@mit.edu (M. Balcells), marta.pegueroles@upc.edu (M. Pegueroles), andres.garcia@iqs.url.edu (A.A. García-Granada).

https://doi.org/10.1016/j.matdes.2024.113395
Received 5 September 2024; Received in revised form 4 October 2024; Accepted 20 October 2024
Available online 21 October 2024

challenges. Current trends include new polymeric materials, thinner struts combined with appropriate mechanical properties, radiopacity, and optimized local drug delivery [14]. This pursuit has led to innovations such as the poly(L-lactide-co-ε-caprolactone) (PLCL) polymeric stent design fabricated using a material extrusion-based additive manufacturing technique known as solvent-cast direct-writing (SC-DW) [15,16,17].

Due to the polymeric nature of BRS, significant attention has been directed towards their mechanical performance and its characterization with diverse experimental methods [18]. Due to the small scale of the stent structure and the resource-intensive nature of the prototyping process, Finite Element Analysis (FEA) has evolved into a common research tool for evaluating stent properties, both for mechanical performance [19,20,21,22,23], and interaction with tissues [24,25,26].

Engineering alternative geometries and manufacturing techniques, such as the PLCL SC-DW scaffold, necessitates proper mechanical assessment [27,28,29]. Despite the increase in the number of studies carried out in the BRS field in recent years [30,31], there is scarcity of experimental and computational studies that characterize the force exerted by implantable devices across a wide range of working diameters and extract the most common mechanical properties for polymeric stents, namely parallel and radial crush resistance.

This study explores the implantation dynamics of a self-expanding coronary-sized PLCL SC-DW stent to provide a deep understanding of its mechanical performance by comparing the parallel plate compression method with full compression and expansion using an iris-like device, addressing a gap not previously covered in the literature. Such an approach reveals differences in the stent's mechanical response under varied loading conditions. In addition, this study seeks to validate the computational models by comparing their results with the experimental performance of the PLCL SC-DW stent.

Tensile testing results of solvent-cast PLCL films are provided and adjusted to elastic–plastic curves with yield strains ranging from 2 % to 5 %. The effect of strut dimensions and mechanical properties of the constituent material on stent performance has been analyzed in both parallel and radial tests. These findings offer insights into how a solvent-casted PLCL stent performs under different mechanical loads, aiding in the understanding and prediction of scaffold responses in clinical scenarios. Additionally, the provided information can be used to improve polymeric stent design and evaluation protocols through the optimization of strut dimensions and material properties.

## 2. Materials and methods

### 2.1. Materials formulation

The material used for the fabrication of the polymeric implants was medical grade PLCL, with a 95:5 lactic-to-caprolactone molar ratio, viscosity of 3.8 dl/g, and molecular weight of 700000 g/mol (Corbion, Netherlands). The printable ink was prepared through the dissolution of PLCL pellets in chloroform at a concentration of 12.5 % (w/v). To ensure complete polymer dissolution, a Dual Asymmetric Centrifuge (SpeedMixer™, AC 150.1 FVZ, FlackTek, Germany) was employed. The polymer solution obtained was loaded into 3 cc cartridges (Optimum®, Nordson, USA) to 3D print the stents or poured into a flat Teflon dish to create the films. Both stents and films underwent thermal treatment at 80 °C for 12 h, thus ensuring complete chloroform evaporation [32], and enhancement of mechanical properties [17,33].

### 2.2. Film fabrication and tensile characterization

PLCL solvent-cast manufactured films were cut into 5x30 mm specimens. The tensile testing process was performed with a Bose ElectroForce 3200 (TA Instruments, Denmark). According to ASTM D882-18 [34], a total of 3 specimens were clamped between two toothed hydraulic grippers with a clamping length at the start position of 10 mm. Then, a calibrated load cell of 50 lbf, a preload of 500 mN, and a test speed of 2.5 mm/min were used to pull the specimens. Each sample was characterized by measuring its thickness in three arbitrary points distributed along the length of the film using a micrometer Holex 421850 (Hoffmann Group, USA).

### 2.3. Solvent-cast direct-write stent geometrical design and manufacturing process

The stent design featured a structure comprising rhombic cells, which was created using the computer aided design (CAD) software SolidWorks 2022 (Dassault Systèmes, France). Various adjustable parameters defined the stent's structure, including stent length ($l$), stent diameter ($d$), strut diameter ($t$), number of peaks ($n_p$) and number of revolutions ($n_f$). Stent length was established at 20 mm, stent diameter at 3 mm, strut diameter at 170 μm, number of peaks at 10, and number of revolutions at 1 rev. These parameters, selected for configuring the manufacturing parameters, directly influenced the mechanical properties of the stent [17].

Stents were manufactured using the SC-DW technique employing a 250 μm nozzle (Nordson Corporation, USA). To achieve this, a commercial fused deposition modeling 3D printer (BCN 3D+, BCN 3D technologies, Spain) underwent adaptation to enable the extrusion of the polymeric solution. This adaptation involved replacing the printer's y-axis with a rotating mandrel of adjustable diameter, facilitating the printing of cylindrical monolayer structures, as depicted in Fig. 1 [15].

Manufactured stents were imaged 3 times at 10x using an optical microscope Leica M165 C (Leica Microsystems, Germany) to analyze the stent's joints and surfaces, and to determine the stent's strut size. Stent length was measured using a digital precision caliper (VWR, USA).

For the simulation model, strut thickness and stent length were adjusted based on the actual measurements obtained from the samples. Additionally, a perfectly strut circular cross-section and a 3.0 mm stent diameter were assumed.

### 2.4. Experimental mechanical testing

Two different but complimentary approaches were used to assess the mechanical performance of 3D printed bioresorbable stents: parallel and radial crush resistance. Parallel tests provided information on how stents would react to pinching loads arising from the movement of the deformable arteries, as well as forces produced by external compression. Radial tests indicated how stents would perform in exerting the expanding outward force required to overcome an arterial narrowing and maintain the lumen open for proper blood flow [35].

#### 2.4.1. Crush resistance (parallel)

The parallel crush resistance of a total of 5 printed stents was assessed through a parallel plate compression test using a BOSE ElectroForce 3200 (TA Instruments, Denmark). The whole process was performed at room temperature. According to ISO 25539-2[36], the distance between the parallel plates was adjusted to a known distance (~ 3000 μm). A sample was placed on the support plate in the orientation anticipated to have the least amount of crush resistance. Stents were compressed up to 50 % reduction in diameter between the two flat plates, with the upper plate advancing towards the lower one at 1.0 mm/min. Finally, stents were decompressed at the same rate until the upper plate reached its initial position. Normal force was measured and normalized by the respective stent length.

#### 2.4.2. Crush resistance (radial)

The radial crush resistance of a total of 3 printed stents was assessed using a TTR2 Tensile Testing Machine for Radial Force with RLU124 Large TwinCamTM Compression Station with Blockwise Radial Force Software (Blockwise, USA). The whole process was performed at room

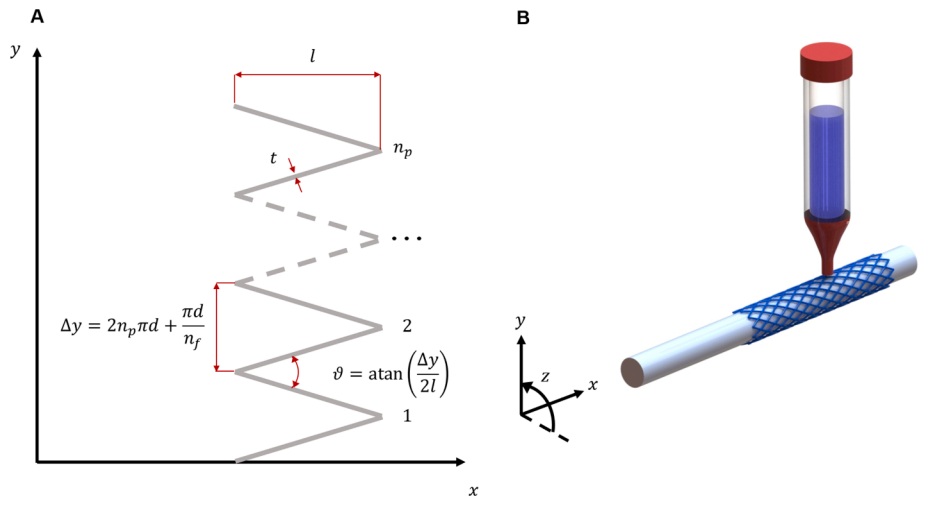


**Fig. 1.** Integrated visualization of polymeric stent design through solvent-cast direct writing technique. A. geometrical design equations and parameters. B. 3D rendering of the implant conformation procedure. .
Adapted from Chausse et al. [15]

temperature. According to ISO 25539-2 [36], sufficient clearance (> 3500 μm) was created by opening the aperture of the radial force test apparatus. A sample was inserted into the radial force test equipment and loaded beyond the point required for clinically significant deformation (2000 μm for 33 % compression) using a uniform rate of compression (1.0 mm/min). Finally, the sample was unloaded using the same uniform rate until sufficient clearance (> 3500 μm) was reached. The radial strength was determined by utilizing the corresponding load-versus-diameter curve and normalized by the respective stent length.

### 2.5. FEA mechanical testing

The consistent units that were used for the definition of the corresponding simulation models are summarized in Table 1:

The stent mesh was generated from a seed size of 0.2 mm, with a curvature control defined by a maximum deviation factor of 0.05 (h/L) and a minimum size control governed by a fraction of the overall size of 0.2. This ensured a proper adjustment of the mesh to the discretized struts' circular cross-section, as shown in Fig. 2. The element type used was the C3D10M (10-node modified quadratic tetrahedron). This mesh definition ensured sufficient quality to capture the bending stresses that exist during the device compression process. A set was generated with two centric nodes on which a boundary condition was applied to fix the geometry in space. A section property was assigned with the section type Solid Homogeneous. The constitutive material for the definition of the stent was defined according to the material properties obtained from the mechanical characterization of the biodegradable polymer PLCL. A density of 1.5E-9 ton/mm$^3$ and a Poisson's coefficient of 0.3 [18,37,38] were defined, along with the elastic and plastic stress–strain curve of the polymer. Four distinct constitutive materials with yield strain values ranging from 2 % to 5 % were defined.

The geometry of each of the compression plates was generated within the same Abaqus CAE Explicit software. Each plate was defined as a 10x30 mm 2D planar shell surface. A reference point was set at the center of the lower 10 mm edge. The plaque mesh was generated from a seed size of 1.0 mm, with a curvature control defined with a maximum deviation factor of 0.1 (h/L) and a minimum size control governed by a fraction of the overall size of 0.1. The element type used was the S4R (4-node doubly curved thin or thick shell, reduced integration, hourglass control, finite membrane strains). A set was generated for the reference point on which the boundary condition was applied to displace the geometry in space. A section property was assigned with the section type Shell Homogeneous. The constitutive material for the definition of the rigid plate was not taken into account due to the application of a rigid body constraint that prevented their deformation.

The previously mentioned parts were assembled in such a way that there was a minimum gap between the stent and each of the plates, as shown in Fig. 3 and Fig. 4.

The simulation was divided into 2 steps:

- Compression step: The rigid plates were used to compress the stent to the desired minimum diameter.
- Expansion step: The rigid plates were used to allow the stent to slowly expand until it reached its equilibrium state, which corresponded to its initial shape in the case of elastic recovery.

The total simulated time was 0.0028 s for the whole testing process, such that ½ corresponded to the crimping step and ½ corresponded to the expansion step. Monitoring of internal and kinetic energies ensured that the kinetic energy remained consistently below 5 % of the internal energy at all times during the testing procedure[35].

Explicit integration methods are considered conditionally stable. This is because the lowest stable time increment (STI), $\Delta t$, must be lower than a critical STI, $\Delta tcrit$ [39,40,41]. Considering the characteristics of the particular model, the mass scaling was applied semi-automatically every 1000 increments to the whole model by setting a target time increment of 2E-8 s. Hard contact between the outer surface of the stent and the inner surface of the rigid plates was specified with a friction coefficient of 0.4, ensuring that there was no slippage between the stent and the rigid plates [18,38,42,43,44]. The same property was defined for the self-contact of the stent surfaces, ensuring that they did not penetrate each other.

Finally, a displacement boundary condition was applied to each of the parallel plates to reduce the stent diameter from 3.0 mm to 2.0 mm during the compression step and to increase the stent diameter from 2.0 mm to 3.0 mm during the expansion step.

**Table 1**
Consistent units used in the simulation model.

| Dimension | Length | Force | Mass | Time | Stress | Energy | Density |
|---|---|---|---|---|---|---|---|
| Units | mm | N | tone | s | MPa | mJ | tone/mm$^3$ |

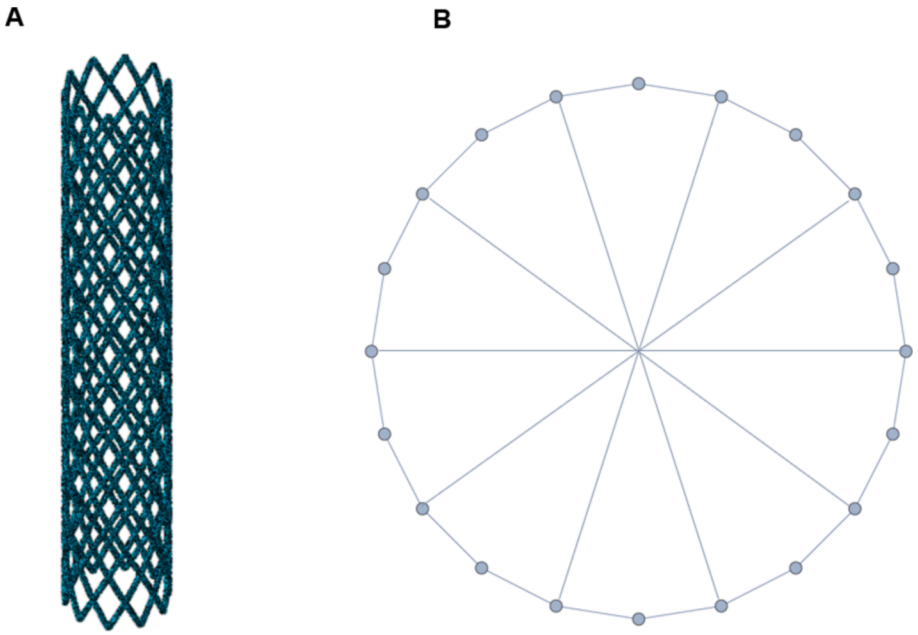


**Fig. 2.** Stent geometric configuration and mesh definition using C3D10M elements in Abaqus CAE. A. Overall stent mesh visualization. B. Consistency and curvature control visualization of the elements and nodes for the definition of the stent struts' cross-section.

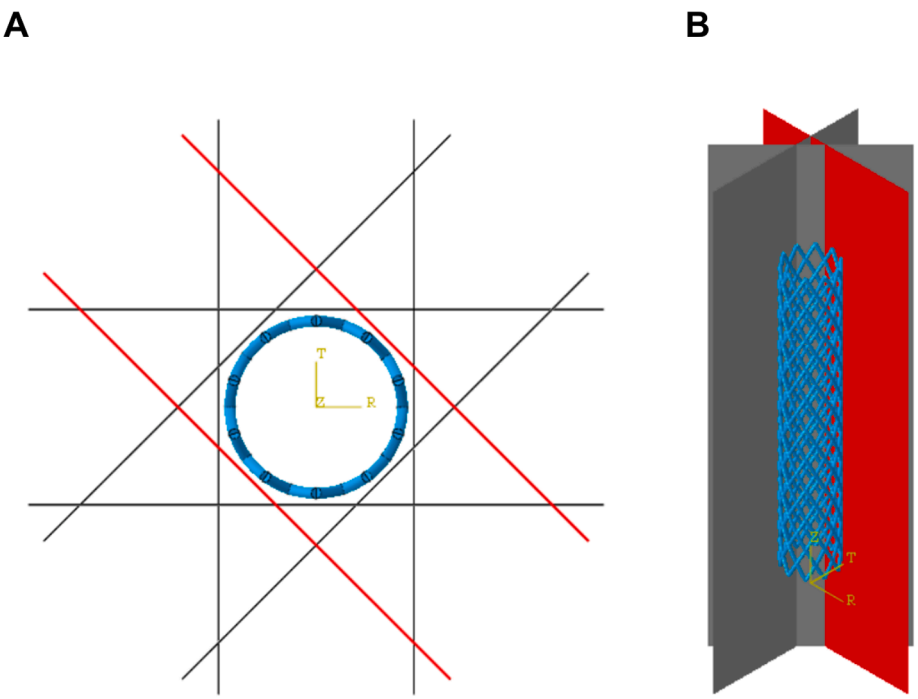


**Fig. 3.** Stent and plaques system's assembly for crush resistance testing within the FEM software. A. Top view. B. Isometric view. Crush resistance (parallel) analysis is solely defined with red-colored plaques.

## 3. Results and discussion

### 3.1. PLCL films mechanical characterization

PLCL films with a thickness of 130 ± 5 μm were obtained. Tensile testing of the solvent-cast films resulted in a stress–strain curve with a first elastic region reaching a stress of 53.3 ± 4.2 MPa, followed by an extended plasticization region. Constituent material setup in the simulation model required the distinction between the elastic and plastic regions of the material [45,46]. For this purpose, different yield strain values were defined between 2 % and 5 %. Young's modulus was calculated as the ratio between yield stress and its corresponding yield strain, as shown in Fig. 5.

The elastic region of the material is not perfectly linear within the range of 5 % strains, but it can be closely approximated by yield strain and Young's modulus, as suggested by Qiu *et al.* [38]. In addition, the Young's modulus and yield stress resulting from the tensile test are consistent with the elastic–plastic behavior of the polymeric material [47,48].

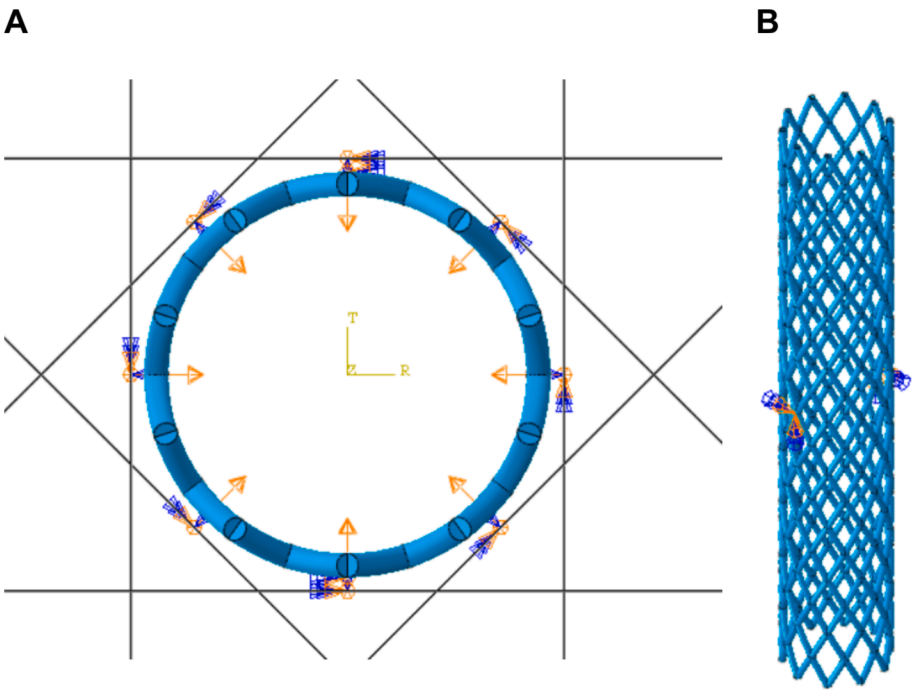


**Fig. 4.** Boundary conditions assignment to the parts of the crush resistance testing assembly. A. Compression plates' displacement conditions applied to each corresponding rigid body's reference point. B. Stent's movement constraint applied to two central nodes within the defined geometry.

### 3.2. Stent manufacturing outcomes and geometrical properties

The first batch of stents, dedicated to parallel crush resistance testing, had strut thickness of 166 ± 12 μm and implant length of 22 ± 1 μm. The second batch, dedicated to radial crush resistance testing, had slightly thicker struts (190 ± 10 μm) and same length (23 ± 1 μm). These values align closely with the working range of numerous CE-marked bioresorbable scaffolds [12]. Crush resistance of a stent is highly influenced by the physical properties of its geometry and its manufacturing process [49]. Therefore, stent dimensions must be strongly considered to properly assess the resistance presented by the different samples undergoing the compression process [50,51]. Analyzing the forces and stresses across various diameters allows for adjustments in design parameters, such as reducing strut diameters to meet specific force requirements for patients. This versatility is achievable with the SC-DW fabrication method used in this study.

The connections between stent struts displayed a dynamic mesh of filaments, as shown in Fig. 6, showcasing the flexibility and adaptability of the structure. Struts are welded into each other as the solvent material is evaporated through the manufacturing process, as previously reported by Chausse *et al.* [15,17]. These features, inherent to the manufacturing process, underline the precision required for polymeric stents' crafting [51], and provide avenues for ongoing improvement and innovation in stent design and fabrication.

### 3.3. Stent crush resistance (parallel)

The focus for BRS mechanical characterization often lies on assessing specific force values during the stent compression and decompression processes. Typically, results are established at the device's crossing profile or target vessel diameter [52,53,54,55]. However, it is becoming increasingly clear that solely analyzing isolated points may miss crucial insights into stent mechanical performance, potentially leading to misleading conclusions in device development and optimization [56,57]. Therefore, beyond the conventional approach of examining crush resistance at specific crimp diameters, it is key to delve deeper into the entire range of implant working diameters.

The experimental assessment of crush resistance between parallel plates revealed the force exerted by stents at the maximum compression point, ranging between 0.06 N/mm and 0.11 N/mm, in accordance to previously reported poly(L-lactide) [17] and nitinol [55] scaffolds. Lower force values corresponded to smaller strut diameters (green), while higher forces were associated with larger strut diameters (blue), as observed in Fig. 7. This underscores the importance of precise and consistent manufacturing processes to reduce variability across samples [58]. Given that the inertial effects of the struts cross-section diameter are quadratic in nature, one would expect the observed variability among the samples analyzed [59].

The simulation model outcomes, based on a strut thickness of 166 μm matching the samples' dimensions, showed notable discrepancies in crush resistance across tests with different constitutive materials. An increase in strength is observed as the yield strain decreases. This occurs because the decrease in yield strain leads to an increase in Young's modulus [60], thereby strengthening the structure within the elastic behavior range.

Comparing experimental and computational results of the stent crush resistance revealed that underestimating yield strain leads to deviations in the simulation results from the stent's actual behavior. This effect is associated with the deformation suffered by the model during the compression process. Data suggest that, for this specific material, geometry and manufacturing method, the most accurate approach is to use the highest yield strain value, corresponding to a plasticization strain of 5 %.

When examining a specific region of the stent, the stress only reaches meaningful values (> 50 MPa) in very localized areas, rendering the model's plastic deformation negligible, as shown in Fig. 8 (further detail of the results corresponding to different elastic properties can be found in Figure S 1). These areas correspond to the connection point between the different struts that form the meshed structure. This suggests that stents subjected primarily to parallel loads, such as those caused by external compression, are unlikely to experience significant plastic deformation. Consequently, scaffold design must focus on strengthening the structure rather than enhancing its deformability.

In a computational model, various parameters such as geometry

A

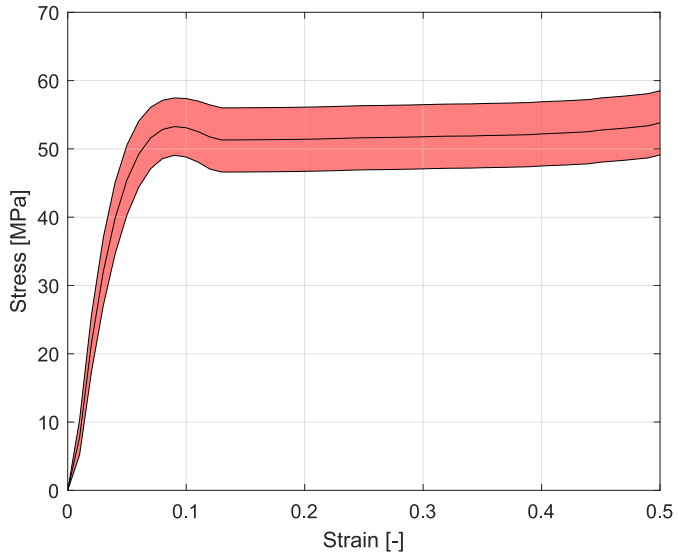


B

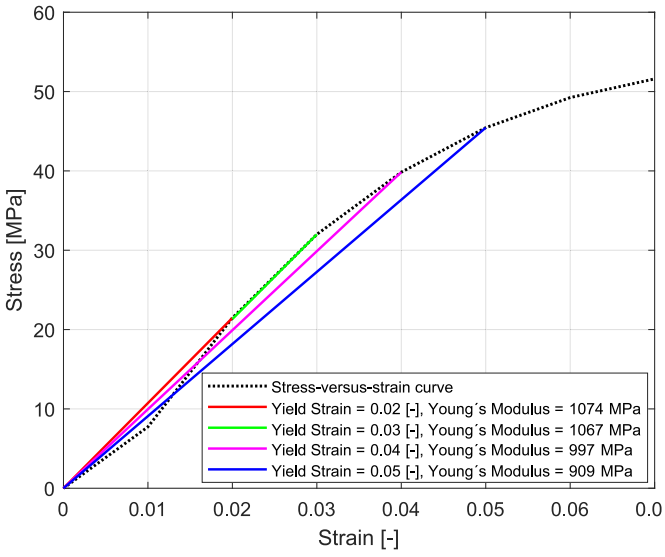


C

| Yield strain [-] | Yield stress [MPa] | Young's Modulus [MPa] |
|---|---|---|
| 0.02 | 21.48 | 1074 |
| 0.03 | 32.01 | 1067 |
| 0.04 | 39.88 | 997 |
| 0.05 | 45.45 | 909 |

**Fig. 5.** Mechanical characterization of PLCL (95:5 lactic-to-caprolactone molar ratio) solvent-cast films via tensile testing. A. Averaged stress–strain curve of the stent's constitutive material. B. Detail of the copolymer elastic properties based on the assumed yield strain values. C. Elastic properties' parameters used for the constitutive material definition in FEA software.

dimensions, friction coefficients, and boundary conditions, must be accurately defined to reflect the actual system. The material properties also need to be determined based on mechanical testing [61]. However, identifying the exact yield strain, where the material transitions from elastic to plastic behavior, may be challenging. The stress–strain curve of semicrystalline polymers such as PLCL typically shows a gradual transition rather than a discrete point. This study focused on evaluating the effects of varying the yield strain between 2 % and 5 % on crush resistance and structural stresses. This approach acknowledged the inherent variability in defining material properties within a simulation. It is also essential to compare experimental and computational results throughout the entire compression and expansion process. The validation of *in silico* results is often overlooked in the existing literature for new-generation BRS [62,63,64]. As observed in Fig. 7, the difference between computational and experimental results varies depending on the diameter at which the normal force is assessed. For this particular analysis, the error between the simulation model using 5 % yield strain and the average of samples having larger strut diameters (blue) was 3.4 % at 2.5 mm, 0.5 % at 2.0 mm and 16.1 % at 1.5 mm of stent crimping diameter.

### 3.4. Stent crush resistance (radial)

The results obtained from the crush resistance (radial) experiments, illustrated in Fig. 9, showcase a high consistency across different samples. The computational model with a 5 % yield strain closely matched the experimental results in the parallel plate test, so this plasticization strain value served as a reference for comparison in the radial plate test. More specifically, the error between the computational model and the averaged experimental results was 1.5 % at 2.5 mm and 7.2 % at 2.0 mm of stent compression. However, more significant discrepancies were observed during stent decompression as the outward expansion force approached 0 N/mm, which were attributed to the material's viscoelastic behavior.

The experimental force-diameter curves show a steep slope in the initial loading phase. The curves smooth out as they reach an implant diameter of 2.0 mm. Subsequently, the unloading curves approach 0 N/mm around 2.8 mm in diameter. This behavior is mirrored in the simulation model, in which a strut thickness of 190 μm was used. The computational results of the stent do not only reflect the same phases but also exhibit remarkably similar radial force values.

From the radial force analysis, it is evident that the stent does not fully recover its initial diameter after crimping and expansion. The

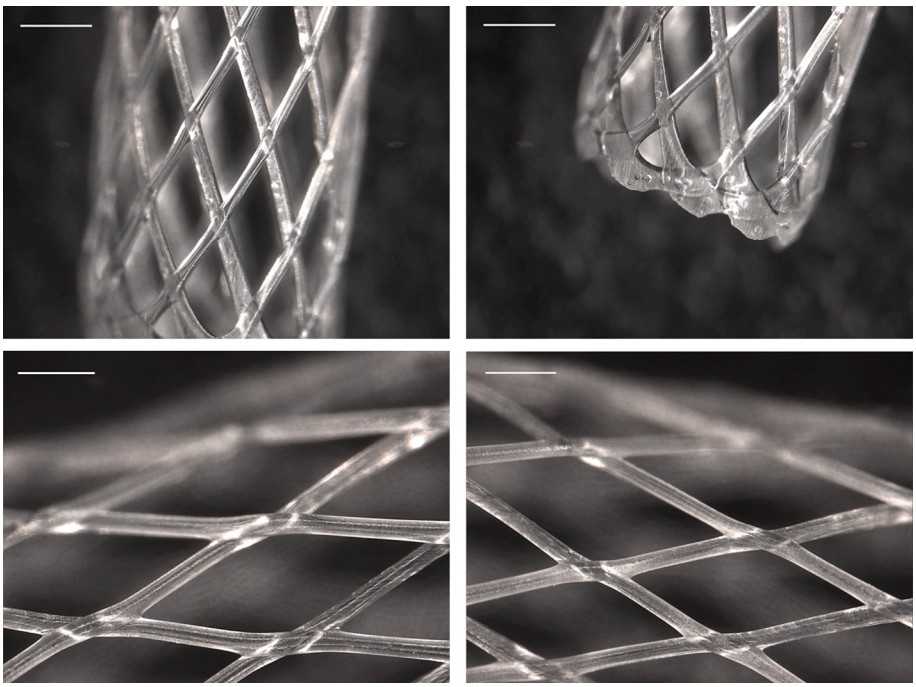

**Fig. 6.** Optical visualization of the SC-DW PLCL manufactured stents using a Leica M165 C. Scale bar = 500 μm.

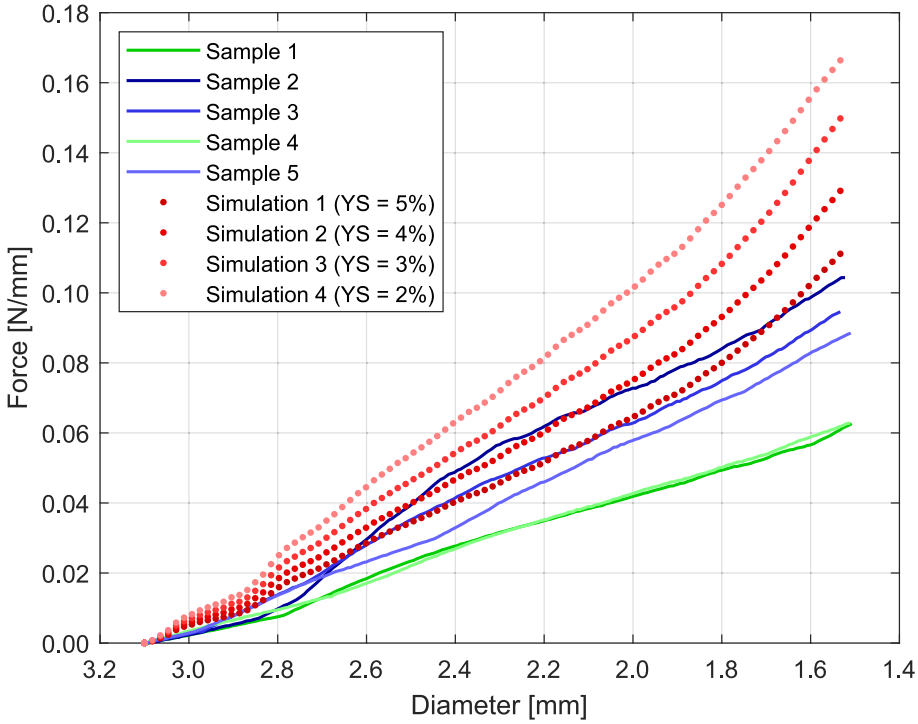


**Fig. 7.** Crush resistance (parallel) for the experimental and computational analyses. Computational stent geometrical model defined with a strut thickness of 166 μm and elastic properties with a yield strain ranging from 2 % to 5 %.

incomplete elastic recovery, at almost 90 %, is due to the higher level of plasticization during the compression process using an iris-like device [65]. This effect was not observed in the compression between parallel plates. Such elastic recovery rates were higher than those corresponding to previously reported poly(L-lactide) and poly(ε-caprolactone) BRS [66], but similar to 4D printed shape memory vascular scaffolds [67], highlighting the self-expansion capabilities of the scaffold [68,69,70,71].

The simulation model indicates certain areas of stress concentration in which high values of plastic deformation occur. High plasticization affects the structure's ability to regain its initial shape after the radial compression process, as shown in Fig. 10 (further detail of the results corresponding to different elastic properties can be found in Figure S 2). Although high strains in the simulation model do not result in fracture points, due to their compressive and very localized nature (as shown in Figure S 3), they do pose potential concerns for stent performance [72].

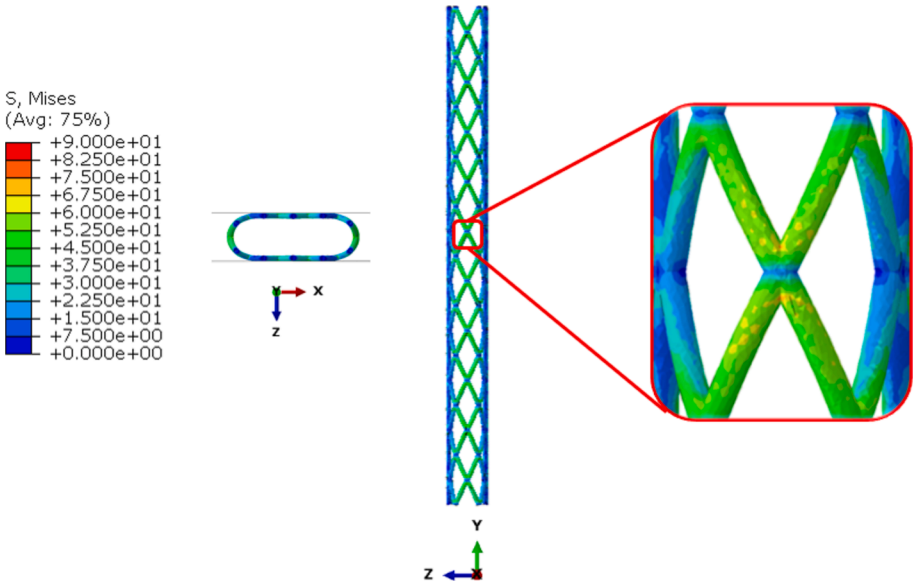


**Fig. 8.** Von Mises stress of high-stress concentration region corresponding to the connection point between two intersecting struts of the stent [MPa]. Computational stent geometrical model defined with a strut thickness of 166 μm and elastic properties with a yield strain of 5 %.

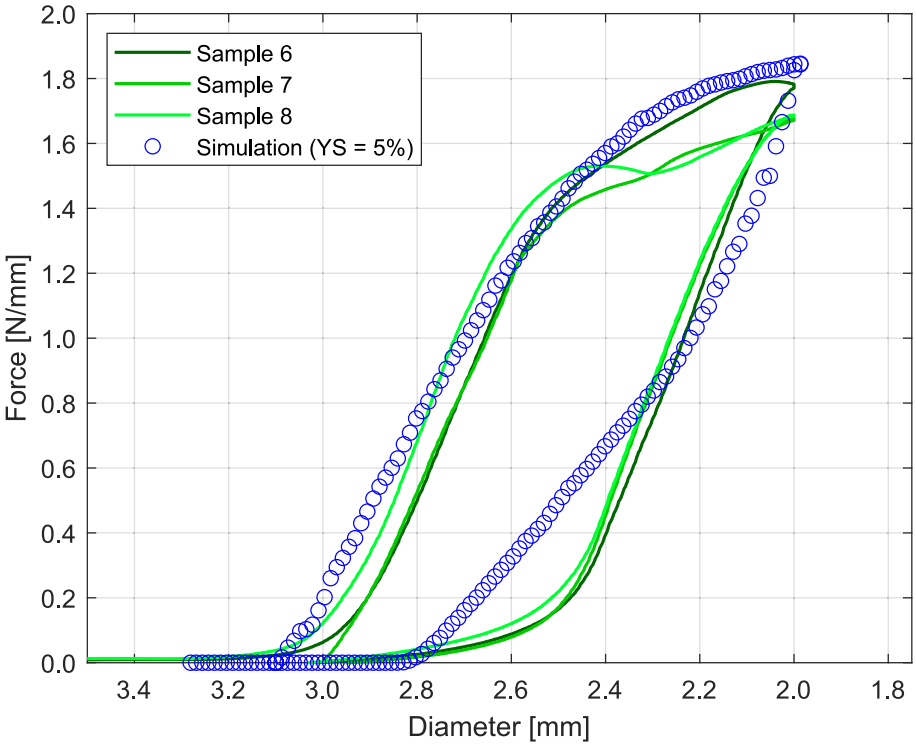


**Fig. 9.** Crush resistance (radial) for the experimental and computational analyses. Computational stent geometrical model defined with a strut thickness of 190 μm and elastic properties with a yield strain of 5 %.

Fig. 11 demonstrates how the mechanical performance of the stent varies based on the definition of these features. This ability to adjust design parameters and analyze the structure in detail could well explain the recent rise in the use of simulation models to study BRS [73,74].

During the compression phase, the stent's behavior shows a slight variation in resistance based on the properties of the stent's constitutive material. More specifically, a lower yield strain (and therefore higher Young's modulus) correlates with a greater resistance of the implant throughout the compression phase. Conversely, the decompression behavior of the stent suggests that a higher yield strain leads to improved resistance and better recovery of the stent's diameter. This is closely related to the material's plasticization strain, as materials with higher plasticization points experience less plastic deformation during crimping, thereby facilitating better recovery [75].

The interpretation of the elastic and plastic properties (yield strain and Young's modulus) derived from the material characterization tests significantly affects the mechanical performance of stents in computational models. This impact is evident not only in the crush resistance of the stent at a specific diameter but also in the behavior of the device over the entire range of working diameters. As well as in the parallel plate

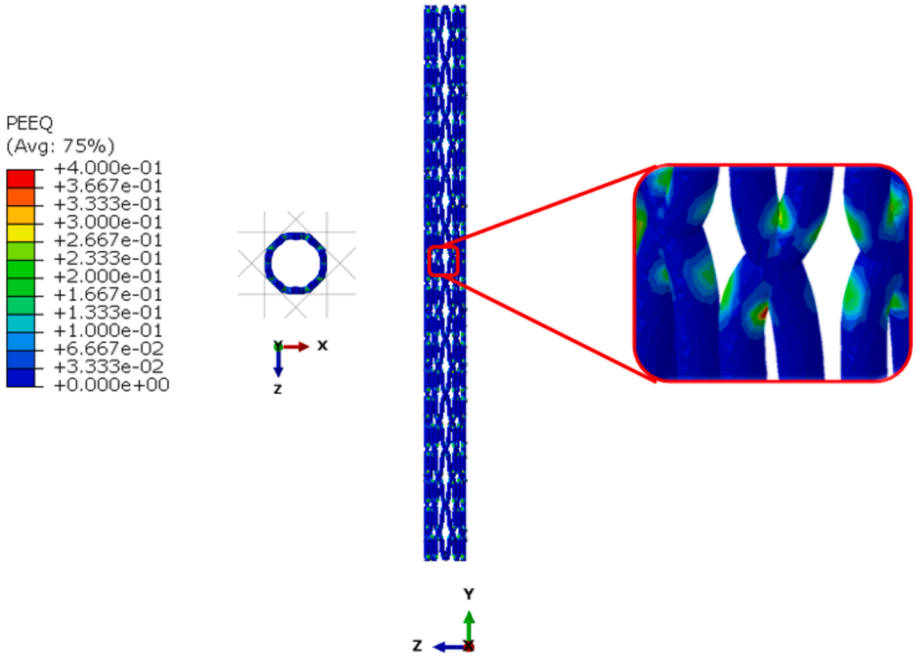


**Fig. 10.** Equivalent plastic strain of high-stress concentration region corresponding to the connection point between two intersecting struts of the stent [-]. Computational stent geometrical model defined with a strut thickness of 190 μm and elastic properties with a yield strain of 5 %.

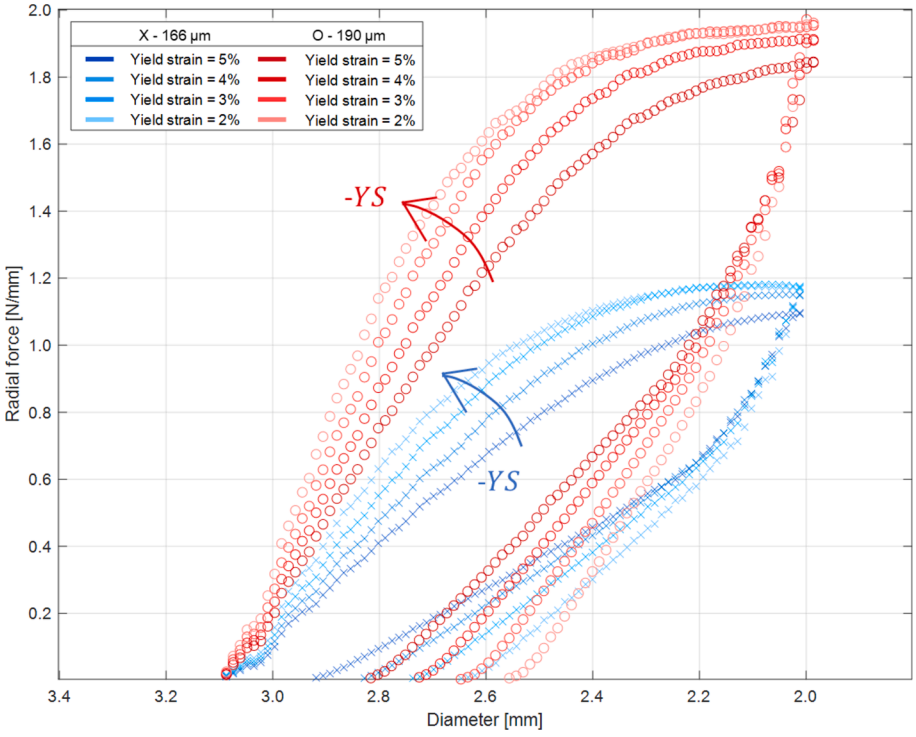


**Fig. 11.** Crush resistance (radial) computational analysis of the computational stent with different strut thicknesses and constitutive material's elastic properties definition

test, a yield strain of 5 % provides the best match between computational and experimental results in the radial compression test.

Such findings have critical implications for future BRS designs. By addressing high plastic strains and tailoring materials for optimal yield strain and elasticity, future designs can prevent long-term complications such as fractures, incomplete shape recovery, and loss of vessel support. Additionally, a deeper understanding of how the constituent material properties (Young's modulus, yield strain) affect the scaffold's mechanical behavior may contribute to deliver patient-specific customized BRS.

## 4. Conclusions

Stent mechanical characterization should be performed across the entire range of working diameters, as crush resistance, shape recovery, and stress distribution, depend on diameter. The presented study found

that PLCL stents manufactured by SC-DW exhibited consistent linear behavior in parallel compression tests, indicating that they operate within an elastic regime with negligible plastic deformation. In contrast, the stents' radial crush resistance showed non-linear behavior, with a response highly dependent on crimp diameter, and significant plasticization during radial compression. This study concludes that differing responses in parallel versus radial performance underscore the complexity of stent behavior under varied mechanical loads. The findings were supported by FEA simulations which, performed at 5 % yield strain, identified areas with high plastic strains. These high plastic strains may lead to poor stent performance post-implantation, such as incomplete shape recovery, loss of wall support, unexpected fractures and reduced lumen patency.

## CRediT authorship contribution statement

**Francesc Canalejo-Codina:** Writing – original draft, Investigation, Conceptualization. **Mariola Cano-Morenilla:** Investigation. **Jordi Martorell:** Project administration, Funding acquisition. **Mercedes Balcells:** Resources. **Marta Pegueroles:** Resources. **Andrés A. García-Granada:** .

## Declaration of competing interest

The authors declare that they have no known competing financial interests or personal relationships that could have appeared to influence the work reported in this paper.

## Acknowledgements

This work was supported by the Agency for Administration of University and Research Grants (AGAUR) of the Generalitat de Catalunya (2021SGR-01368) and the Spanish Government, MCIN/AEI/10.13039/501100011033/FEDER (PID2021-124868OB-C22). Francesc Canalejo has been financed to perform all experiments at Hardvard-MIT Biomedical Engineering Center by Fundació Privada Daniel Bravo Andreu.

## Data availability

Data will be made available on request.

## References

[1] G.M. Baer, et al., Fabrication and in vitro deployment of a laser-activated shape memory polymer vascular stent, Biomed. Eng. Online 6 (43) (2007) Nov, https://doi.org/10.1186/1475-925X-6-43.
[2] Hendra Hermawan, Diego Mantovani, New generation of medical implants: metallic biodegradable coronary stent, in: International Conference on Instrumentation, Communications, Information Technology, and Biomedical Engineering, 2011.
[3] F. Amin, M.N. Ali, U. Ansari, M. Mir, M.A. Minhas, W. Shahid, Auxetic coronary stent endoprosthesis: fabrication and structural analysis, J Appl Biomater Funct Mater 13 (2) (Apr. 2015) E127–E135, https://doi.org/10.5301/jabfm.5000213.
[4] S. Borhani, S. Hassanajili, S.H. Ahmadi Tafti, S. Rabbani, Cardiovascular stents: overview, evolution, and next generation, Prog Biomater 7(3) (2018) 175–205, doi: 10.1007/s40204-018-0097-y.
[5] R. Hoffmann, et al., Patterns and mechanisms of in-stent restenosis: a serial intravascular ultrasound study, Circulation 94 (6) (1996) 1247–1254, https://doi.org/10.1161/01.CIR.94.6.1247.
[6] P.C. Gordon, C.M. Gibson, D.J. Cohen, J.P. Carrozza, R.E. Kuntz, D.S. Baim, Mechanisms of restenosis and redilation witiin coronary stents-quantitative angiographic assessment, J. Am. Coll. Cardiol. 21 (5) (1993) 1166–1174.
[7] D.L. Fischman, et al., A randomized comparison of coronary-stent placement and balloon angioplasty in the treatment of coronary artery disease, N. Engl. J. Med. 331 (8) (1994) 496–501.
[8] C. Spaulding, J. Daemen, E. Boersma, D.E. Cutlip, P.W. Serruys, A pooled analysis of data comparing sirolimus-eluting stents with bare-metal stents, N. Engl. J. Med. 356 (10) (Mar. 2007) 989–997, https://doi.org/10.1056/nejmoa066633.
[9] C. Stettler, et al., Outcomes associated with drug-eluting and bare-metal stents: a collaborative network meta-analysis, Lancet 370 (9591) (Sep. 2007) 937–948, https://doi.org/10.1016/S0140-6736(07)61444-5.
[10] A. Abizaid, J.R. Costa, New drug-eluting stents an overview on biodegradable and polymer-free next-generation stent systems, Circ. Cardiovasc. Interv. 3 (4) (Aug. 2010) 384–393, https://doi.org/10.1161/CIRCINTERVENTIONS.109.891192.
[11] B. Nečemer Donik, S. Glodež, J. Kramberger, Finite element analysis of the mechanical performance of a two-layer polymer composite stent structure, Eng Fail Anal 137 (2022) 106267, doi: 10.1016/J.ENGFAILANAL.2022.106267.
[12] H. Jinnouchi, S. Torii, A. Sakamoto, F.D. Kolodgie, R. Virmani, A.V. Finn, Fully bioresorbable vascular scaffolds: lessons learned and future directions, Nat. Rev. Cardiol. 16 (5) (May 2019) 286–304, https://doi.org/10.1038/s41569-018-0124-7.
[13] P.J. Wang, N. Ferralis, C. Conway, J.C. Grossman, E.R. Edelman, Strain-induced accelerated asymmetric spatial degradation of polymeric vascular scaffolds, Proc. Natl. Acad. Sci. 115 (11) (2018) 2640–2645, https://doi.org/10.1073/pnas.1716420115.
[14] M.I. Okereke, R. Khalaj, A.G. Tabriz, D. Douroumis, Development of 3D printable bioresorbable coronary artery stents: a virtual testing approach, Mech. Mater. 163 (Dec. 2021) 104092, https://doi.org/10.1016/J.MECHMAT.2021.104092.
[15] V. Chausse, E. Casanova-Batlle, C. Canal, M.P. Ginebra, J. Ciurana, M. Pegueroles, Solvent-cast direct-writing and electrospinning as a dual fabrication strategy for drug-eluting polymeric bioresorbable stents, Addit. Manuf. 71 (Jun. 2023), https://doi.org/10.1016/j.addma.2023.103568.
[16] V. Chausse, C. Iglesias, E. Bou-Petit, M.P. Ginebra, M. Pegueroles, Chemical vs thermal accelerated hydrolytic degradation of 3D-printed PLLA/PLCL bioresorbable stents: characterization and influence of sterilization, Polym. Test. 117 (Jan. 2023), https://doi.org/10.1016/j.polymertesting.2022.107817.
[17] V. Chausse, et al., Solvent-cast direct-writing as a fabrication strategy for radiopaque stents, Addit. Manuf. 48 (Dec. 2021), https://doi.org/10.1016/j.addma.2021.102392.
[18] A. Schiavone, T.Y. Qiu, L.G. Zhao, Crimping and deployment of metallic and polymeric stents – finite element modelling, Vessel plus 1 (2017) 12–21, https://doi.org/10.20517/2574-1209.2016.03.
[19] K. Mori, T. Saito, Effects of stent structure on stent flexibility measurements, Ann. Biomed. Eng. 33 (6) (Jun. 2005) 733–742, https://doi.org/10.1007/s10439-005-2807-6.
[20] L. Petrini, F. Migliavacca, F. Auricchio, G. Dubini, Numerical investigation of the intravascular coronary stent flexibility, J. Biomech. 37 (4) (Apr. 2004) 495–501, https://doi.org/10.1016/j.jbiomech.2003.09.002.
[21] A.R. Pelton, V. Schroeder, M.R. Mitchell, X.Y. Gong, M. Barney, S.W. Robertson, Fatigue and durability of Nitinol stents, J. Mech. Behav. Biomed. Mater. 1 (2) (Apr. 2008) 153–164, https://doi.org/10.1016/j.jmbbm.2007.08.001.
[22] F. Gervaso, C. Capelli, L. Petrini, S. Lattanzio, L. Di Virgilio, F. Migliavacca, On the effects of different strategies in modelling balloon-expandable stenting by means of finite element method, J. Biomech. 41 (6) (2008) 1206–1212, https://doi.org/10.1016/j.jbiomech.2008.01.027.
[23] D.E. Kiousis, A.R. Wulff, G.A. Holzapfel, Experimental studies and numerical analysis of the inflation and interaction of vascular balloon catheter-stent systems, Ann. Biomed. Eng. 37 (2) (Feb. 2009) 315–330, https://doi.org/10.1007/s10439-008-9606-9.
[24] C. Capelli, F. Gervaso, L. Petrini, G. Dubini, F. Migliavacca, Assessment of tissue prolapse after balloon-expandable stenting: influence of stent cell geometry, Med. Eng. Phys. 31 (4) (May 2009) 441–447, https://doi.org/10.1016/j.medengphy.2008.11.002.
[25] C. Lally, F. Dolan, P.J. Prendergast, Cardiovascular stent design and vessel stresses: a finite element analysis, J. Biomech. 38 (8) (2005) 1574–1581, https://doi.org/10.1016/j.jbiomech.2004.07.022.
[26] I. Pericevic, C. Lally, D. Toner, D.J. Kelly, The influence of plaque composition on underlying arterial wall stress during stent expansion: the case for lesion-specific stents, Med. Eng. Phys. 31 (4) (May 2009) 428–433, https://doi.org/10.1016/j.medengphy.2008.11.005.
[27] A. Emelogu, M. Marufuzzaman, S.M. Thompson, N. Shamsaei, L. Bian, Additive manufacturing of biomedical implants: a feasibility assessment via supply-chain cost analysis, Addit. Manuf. 11 (Jul. 2016) 97–113, https://doi.org/10.1016/j.addma.2016.04.006.
[28] A. Mitchell, U. Lafont, M. Hołyńska, C. Semprimoschnig, A review of 4D printing and future applications, Addit. Manuf. 24 (Dec. 2018) 606–626, https://doi.org/10.1016/j.addma.2018.10.038.
[29] L. Wang, L. Jiao, S. Pang, P. Yan, X. Wang, T. Qiu, The development of design and manufacture techniques for bioresorbable coronary artery stents, Micromachines (Basel) 12 (8) (2021) Aug, https://doi.org/10.3390/mi12080990.
[30] A. Kapoor, N. Jepson, N.W. Bressloff, P.H. Loh, T. Ray, S. Beier, The road to the ideal stent: a review of stent design optimisation methods, findings, and opportunities, Mater. Des. 237 (Jan. 2024) 112556, https://doi.org/10.1016/J.MATDES.2023.112556.
[31] R.A. Sahu, A. Nashine, A. Mudey, S.A. Sahu, R. Prasad, Cardiovascular stents: types and future landscape, Cureus 15 (8) (2023) Aug, https://doi.org/10.7759/CUREUS.43438.
[32] R. Schieber, et al., Functionalization strategies and fabrication of solvent-cast PLLA for bioresorbable stents, Appl. Sci. (Switzerland) 11 (4) (Feb. 2021) 1–18, https://doi.org/10.3390/app11041478.
[33] N. Jayanth, K. Jaswanthraj, S. Sandeep, N.H. Mallaya, S.R. Siddharth, Effect of heat treatment on mechanical properties of 3D printed PLA, J. Mech. Behav. Biomed. Mater. 123 (Nov. 2021), https://doi.org/10.1016/j.jmbbm.2021.104764.
[34] American Society for Testing and Materials, 'ASTM D882 - 18: Standard Test Method for Tensile Properties of Thin Plastic Sheeting', 2021, [Online]. Available: http://www.ansi.org.

[35] M.S. Cabrera, C.W.J. Oomens, F.P.T. Baaijens, Understanding the requirements of self-expandable stents for heart valve replacement: radial force, hoop force and equilibrium, J. Mech. Behav. Biomed. Mater. 68 (Apr. 2017) 252–264, https://doi.org/10.1016/J.JMBBM.2017.02.006.

[36] The International Organization for Standardization, 'ISO 25539-2: Cardiovascular implants-Endovascular devices: Vascular stents', 2020, [Online]. Available: https://compliancenavigator.bsigroup.com/doc/000000000030385890.

[37] H. Li et al., Design optimization of stent and its dilatation balloon using kriging surrogate model, Biomed. Eng. Online 16(1) (2017), doi: 10.1186/s12938-016-0307-6.

[38] T.Y. Qiu, M. Song, L.G. Zhao, A computational study of crimping and expansion of bioresorbable polymeric stents, Mech Time Depend Mater 22 (2) (May 2018) 273–290, https://doi.org/10.1007/s11043-017-9371-y.

[39] G. Cocchetti, M. Pagani, U. Perego, Selective mass scaling and critical time-step estimate for explicit dynamics analyses with solid-shell elements, Comput. Struct. 127 (2013) 39–52, https://doi.org/10.1016/j.compstruc.2012.10.021.

[40] L.S. Pereira, G.H.B. Donato, M.M. Neto, The effect of mass scaling and speed increase in explicit dynamic simulations using tensile test, in International Nuclear Atlantic Conference, 2021.

[41] F. Ducobu, E. Rivière-Lorphèvre, E. Filippi, On the introduction of adaptive mass scaling in a finite element model of Ti6Al4V orthogonal cutting, Simul. Model. Pract. Theory 53 (2015) 1–14, https://doi.org/10.1016/j.simpat.2015.02.003.

[42] X.L. Ruan, et al., Mechanical design of antichiral-reentrant hybrid intravascular stent, Int. J. Appl. Mech. 10 (10) (2018) Dec, https://doi.org/10.1142/S1758825118501053.

[43] L. Wang, J. Tong, P. Dong, D.L. Wilson, H.G. Bezerra, L. Gu, Mechanical performance of PLLA stent, Design of Medical Devices Conference Am. Soc. Mech. Eng. (Apr. 2018), https://doi.org/10.1115/DMD2018-6957.

[44] Q. Wang, G. Fang, Y. Zhao, G. Wang, T. Cai, Computational and experimental investigation into mechanical performances of Poly-L-Lactide Acid (PLLA) coronary stents, J. Mech. Behav. Biomed. Mater. 65 (Jan. 2017) 415–427, https://doi.org/10.1016/j.jmbbm.2016.08.033.

[45] Y. Baradaran, M. Baghani, M. Kazempour, S.K. Hosseini, M. Karimpour, M. Baniassadi, Design and shape optimization of a biodegradable polymeric stent for curved arteries using FEM, Front. Mech. Eng. 7 (May 2021) 689002, https://doi.org/10.3389/FMECH.2021.689002/BIBTEX.

[46] N. Debusschere, P. Segers, P. Dubruel, B. Verhegghe, M. De Beule, A finite element strategy to investigate the free expansion behaviour of a biodegradable polymeric stent, J. Biomech. 48 (10) (Jul. 2015) 2012–2018, https://doi.org/10.1016/J.JBIOMECH.2015.03.024.

[47] R. Duan, et al., Blending with poly(l -lactic acid) improves the printability of poly (l-lactide- co-caprolactone) and enhances the potential application in cartilage tissue engineering, ACS Omega 6 (28) (Jul. 2021) 18300–18313, https://doi.org/10.1021/ACSOMEGA.1C02190/ASSET/IMAGES/LARGE/AO1C02190_0009.JPEG.

[48] G. Gustafsson, et al., Mechanical characterization and modelling of the temperature-dependent impact behaviour of a biocompatible poly(L-lactide)/poly (ε-caprolactone) polymer blend, J. Mech. Behav. Biomed. Mater. 51 (Nov. 2015) 279–290, https://doi.org/10.1016/J.JMBBM.2015.07.007.

[49] P. Savage, B.P. O'Donnell, P.E. McHugh, B.P. Murphy, D.F. Quinn, Coronary stent strut size dependent stress-strain response investigated using micromechanical finite element models, Ann. Biomed. Eng. 32 (2) (Feb. 2004) 202–211, https://doi.org/10.1023/B:ABME.0000012740.47963.9e.

[50] G.V. Praveen Kumar, L. Mathew, Effects of design parameters on the radial force of percutaneous aortic valve stents, Cardiovasc Revasc Med 11(2) (2010) 101–104, doi: 10.1016/J.CARREV.2009.04.005.

[51] C. Wang, L. Zhang, Y. Fang, W. Sun, Design, characterization, and 3D printing of cardiovascular stents with zero poisson's ratio in longitudinal deformation, Engineering 7 (7) (Jul. 2021) 979–990, https://doi.org/10.1016/J.ENG.2020.02.013.

[52] T. Barkholt, B. Webber, N.R. Holm, J.A. Ormiston, Mechanical properties of the drug-eluting bioresorbable magnesium scaffold compared with polymeric scaffolds and a permanent metallic drug-eluting stent, Catheter. Cardiovasc. Interv. 96 (7) (Dec. 2020) E674–E682, https://doi.org/10.1002/ccd.28545.

[53] W. Schmidt, P. Behrens, C. Brandt-Wunderlich, S. Siewert, N. Grabow, K. P. Schmitz, In vitro performance investigation of bioresorbable scaffolds – standard tests for vascular stents and beyond, Cardiovasc. Revasc. Med. 17 (6) (Sep. 2016) 375–383, https://doi.org/10.1016/j.carrev.2016.05.001.

[54] U. Sharma, et al., The development of bioresorbable composite polymeric implants with high mechanical strength, Nat. Mater. 17 (1) (Jan. 2018) 96–102, https://doi.org/10.1038/NMAT5016.

[55] C. Brandt-Wunderlich, et al., Support function of self-expanding nitinol stents - Are radial resistive force and crush resistance comparable? Curr. Direct. Biomed. Eng. 5 (1) (Sep. 2019) 465–467, https://doi.org/10.1515/cdbme-2019-0117.

[56] E. Galvin, C. Cummins, S. Yoshihara, B. J. Mac Donald, C. Lally, Plastic strains during stent deployment have a critical influence on the rate of corrosion in absorbable magnesium stents, Med Biol Eng Comput, vol. 55, no. 8, pp. 1261–1275, Aug. 2017, doi: 10.1007/S11517-016-1584-8.

[57] K.D. Everett, et al., Structural mechanics predictions relating to clinical coronary stent fracture in a 5 year period in FDA MAUDE database, Ann. Biomed. Eng. 44 (2) (Feb. 2016) 391, https://doi.org/10.1007/S10439-015-1476-3.

[58] W. Jiang, W. Zhao, T. Zhou, L. Wang, and T. Qiu, A review on manufacturing and post-processing technology of vascular stents, Micromachines (Basel) 13(1) (2022), doi: 10.3390/MI13010140.

[59] D. Mulhayatiah, H.Y. Suhendi, R. Zakwandi, Y. Dirgantara, M.A. Ramdani, Moment of inertia: development of rotational dynamics KIT for physics students, IOP Conf Ser Mater Sci Eng 434 (1) (Nov. 2018) 012014, https://doi.org/10.1088/1757-899X/434/1/012014.

[60] R. H. Alasfar, S. Ahzi, N. Barth, V. Kochkodan, M. Khraisheh, M. Koç, 'A review on the modeling of the elastic modulus and yield stress of polymers and polymer nanocomposites: effect of temperature, loading rate and porosity', Polymers (Basel), vol. 14, no. 3, Feb. 2022, doi: 10.3390/POLYM14030360.

[61] J.S. Bergström, D. Hayman, An overview of mechanical properties and material modeling of polylactide (PLA) for medical applications, Ann. Biomed. Eng. 44 (2) (Feb. 2016) 330–340, https://doi.org/10.1007/S10439-015-1455-8.

[62] M. Milosevic, et al., Application of in silico platform for the development and optimization of fully bioresorbable vascular scaffold designs, Front Med Technol 3 (2021), https://doi.org/10.3389/fmedt.2021.724062.

[63] Ž. Donik, B. Nečemer, M. Vesenjak, S. Glodež, J. Kramberger, Computational analysis of mechanical performance for composite polymer biodegradable stents, Materials 14 (20) (2021) Oct, https://doi.org/10.3390/ma14206016.

[64] G. S. Karanasiou et al., Design and implementation of in silico clinical trial for Bioresorbable Vascular Scaffolds', in 42nd Annual International Conference of the IEEE Engineering in Medicine & Biology Society (EMBC), IEEE, Jul. 2020, pp. 2675–2678. doi: 10.1109/EMBC44109.2020.9176317.

[65] D. Moller, W. Reimers, A. Pyzalla, A. Fischer, Residual stresses in coronary artery stents, J. Biomed. Mater. Res. 58 (1) (2001) 69–74, https://doi.org/10.1002/1097-4636(2001)58:1<69::AID-JBM100>3.0.CO;2-9.

[66] A. Thakur, U. K. Vates, S. Mishra, Proof of concept study for radial compression strength & shape memory effect of 3D printed double arrowhead PLA stent, Emergent Mater, pp. 1–12, Jun. 2024, doi: 10.1007/S42247-024-00751-9/TABLES/4.

[67] C. Lin, L.J. Zhang, Y.J. Liu, L.W. Liu, J.S. Leng, 4D printing of personalized shape memory polymer vascular stents with negative Poisson's ratio structure: a preliminary study, Sci. China Technol. Sci. 63 (4) (Apr. 2020) 578–588, https://doi.org/10.1007/S11431-019-1468-2/METRICS.

[68] I. Istif, K. Feratoglu, O.U. Colak, A. Acar, Investigation of tensile, viscoelastic, and viscoplastic behavior of polylactic acid manufactured by fused deposition modeling, J. Test. Eval. 49 (4) (Jul. 2021) 2831–2839, https://doi.org/10.1520/JTE20180964.

[69] A.C. Vieira, J.C. Vieira, R.M. Guedes, A.T. Marques, Degradation and viscoelastic properties of PLA-PCL, PGA-PCL, PDO and PGA fibres, Mater. Sci. Forum 636–637 (2010) 825–832, https://doi.org/10.4028/WWW.SCIENTIFIC.NET/MSF.636-637.825.

[70] M. Balasubramanian, R. Saravanan, V. Shanmugam, Impact of strain rate on mechanical properties of polylatic acid fabricated by fusion deposition modeling, Polym. Adv. Technol. 35 (3) (Mar. 2024) e6335.

[71] K. Upadhyay, D. Spearot, G. Subhash, Validated tensile characterization of the strain rate dependence in soft materials, Int. J. Impact Eng 156 (Oct. 2021) 103949, https://doi.org/10.1016/J.IJIMPENG.2021.103949.

[72] C. Pan, Y. Han, J. Lu, Structural design of vascular stents: a review, Micromachines (Basel) 12(7) (2021), doi: 10.3390/MI12070770.

[73] N. Filipovic, et al., In vitro and in silico testing of partially and fully bioresorbable vascular scaffold, J. Biomech. 115 (Jan. 2021), https://doi.org/10.1016/j.jbiomech.2020.110158.

[74] G. Karanasiou et al., In silico assessment of the effects of material on stent deployment, in: IEEE 17th International Conference on Bioinformatics and Bioengineering (BIBE), IEEE, Oct. 2017, pp. 462–467. doi: 10.1109/BIBE.2017.00-11.

[75] G.M. Swallowe, Yield and plastic deformation, Springer, vol. 3, pp. 281–285, 1999, doi: 10.1007/978-94-015-9231-4_61.